Global magnetohydrodynamic magnetosphere simulation with an adaptively embedded particle-in-cell model

Xiantong Wang[1], **Yuxi Chen**[1], **Gábor Tóth**[1]

[1]Department of Climate and Space Sciences and Engineering, University of Michigan, Ann Arbor, MI, USA

Key Points:

- We perform a global simulation of a geomagnetic storm event with kinetic modeling of the magnetotail reconnection
- The kinetic region is adaptively embedded to the MHD model while the reconnection sites are identified by physical criteria during the runtime
- The global scale, mesoscale and electron scale features are observed in one simulation

Corresponding author: Xiantong Wang, `xtwang@umich.edu`

Abstract

We perform a geomagnetic event simulation using a newly developed magnetohydrodynamic with adaptively embedded particle-in-cell (MHD-AEPIC) model to study by solving the magnetotail reconnection physics better, what's the influence on the simulation results at multiple physical scales. We also present the Hall MHD and ideal MHD simulation results of the same event for comparison. For the global scale features, three models produce very close SYM-H and SuperMag Electrojet Index (SME), which indicates the global magnetic field configurations from three models are very similar to each other. For the mesoscale feature, the MHD-AEPIC and Hall MHD models can produce tailward and earthward fluxropes. However, there is no fluxrope generated at the near-earth current sheet by the ideal MHD model. For the electron scale feature, the MHD-AEPIC can produce a crescent shape distribution of the electron velocity space at the electron diffusion region which is agreed with the MMS observation. The kinetic feature is not available in either Hall MHD or ideal MHD model.

1 Introduction

Geomagnetic storm is a major disturbance of Earth's magnetosphere that occurs when there is a significant amount of energy being deposited into the geospace. Geomagnetic storm usually results in an enhancement of the ring current system that produces magnetic disturbances on the ground (Dessler et al., 1961; Lyons & Williams, 1980; Hamilton et al., 1988). In addition to that, currents produced in the magnetosphere that follow the magnetic field can connect to intense currents in the auroral region which will also cause geomagnetic disturbances (Feldstein et al., 1997). So it is critical to conduct geomagnetic storm simulation to study the underlying physics and evaluate its impacts.

There have been a lot of publications dedicated to study the geomagnetic storm simulation, physics-based models are what we are interested in for this paper. Firstly published in the 1980s (LeBoeuf et al., 1981; Wu et al., 1981; Brecht et al., 1981, 1982), global magnetohydrodynamics (MHD) simulation has been considered as the major tool because of it's self-consistent description of the space plasma. Later on, models applied more advanced algorithms have been developed, such as Lyon-Fedder-Mobarry (LFM) (J. G. Lyon et al., 1986; J. Lyon et al., 2004), the OpenGGCM (Raeder et al., 1995, 1996) and the GUMICS (Grand Unified Magnetosphere Ionosphere Coupling Simulation) model (Janhunen, 1996). In this paper, we use the University of Michigan's Space Weather Modeling Framework (SWMF (Tóth et al., 2012)) which also use a MHD model: Block Adaptive-Tree Solar-wind Roe-type Upwind Scheme (BATS-R-US) (Powell et al., 1999) as its global magnetosphere (GM) component. The SWMF has been applied to many storm event simulations (Tóth et al., 2007; Glocer et al., 2009; Haiducek et al., 2017), which is also been selected as the physics-based model at the Space Weather Prediction Center based on a thorough model comparison (Pulkkinen et al., 2013).

Despite all the successful applications MHD models have achieved, there is one underlying condition that all these MHD models follow: the distribution function of the ions and electrons is assumed to be Maxwellian. Numerous observations suggest that this condition is violated especially near the magnetic reconnection sites (L.-J. Chen et al., 2016; Burch et al., 2016; Hwang et al., 2019; Lotekar et al., 2020). However, the reconnection physics in the MHD models relies on either Hall resistivity, or ad hoc anomalous resistivity, or simply numerical resistivity. Considering magnetic reconnection is one of the essential physical process for transforming the magnetic field energy to the plasma. It is very meaningful to resolve kinetic physics in a global simulation and validate if it is contributing to the geomagnetic disturbances prediction.

As a relatively new feature introduced in the SWMF, the MHD with embedded Particle-In-Cell (MHD-EPIC) model (Daldorff et al., 2014) enables kinetic physics to be introduced in a global MHD background, which also has been successfully used in studying planetary magnetospheres: the interaction between the Jovian wind and Ganymede's magnetopshere (Tóth et al., 2016; Zhou et al., 2019, 2020); the flux transfer events (FTEs) at the Earth's dayside magnetopause (Y. Chen et al., 2017); the Mars' magnetotail dynamics (Y. Ma et al., 2018) and the dawn-dusk asymmetries discovered at the Mercury's magnetotail (Y. Chen et al., 2019). However, the iPIC3D (Markidis et al., 2010), which is the PIC model in the MHD-EPIC can only run on a fixed Cartesian grid, which is not flexible enough to cover the whole domain of interest due to massive computational cost. For example, a very large PIC box would be needed to accommodate the flapping motion (Tsutomu & Teruki, 1976; Volwerk et al., 2013) of the magnetotail current sheet during a geomagnetic storm simulation. It's probably feasible for a short time event but for geomagnetic storms which usually happen for days, the computational cost makes the problem unsolvable.

To tackle this problem, we have developed MHD with Adaptively Embedded PIC (MHD-AEPIC) method. Shou et al. (2021) firstly introduces this idea and verifies that by letting the PIC regions following the movement of the kinetic areas, the numerical solution doesn't change essentially. In this paper, we further improve this method and make it more flexible: 1. The size and shape of the active PIC regions can be adapted during the runtime; 2. The adaptation of the active PIC region is fully automatic. To realize the first feature, instead of iPIC3D, we use the FLexible Exascale Kinetic Simulator (FLEKS) (?, ?) as the PIC model in the SWMF. FLEKS inherits all numerical algorithms from MHD-EPIC, and also accommodates an adaptive PIC grid that allows PIC cells to be turned on and off during the simulation as well as a particle splitting and merging feature to improve the solution, more details can be found in Section 2.2. To realize the second feature, we introduce three physical-based criteria to identify reconnection sites in the magnetotail, see Section 2.3 for details.

In this paper, we firstly embed kinetic physics into a real geomagnetic storm simulation and observe features from the global to electron scale. The computational methods are described in Section 2, the demonstration of the adaptation feature and comparisons between models and observations are shown in Section 3 and we summarize in Section 4.

2 Methods

2.1 Global Magnetosphere Model: BATS-R-US

The Block-Adaptive Tree Solar-wind Roe-type Upwind Scheme (BATS-R-US) is used as the Global Magnetosphere (GM) model in our simulation. In the work presented in this paper, the Hall MHD equations (Tóth et al., 2008) are solved, an explicit-implicit scheme is chosen for time stepping and the Sokolov scheme (Sokolov et al., 1999) with third-order monotonized central (Koren) limiter is used as the numerical flux. The hyperbolic cleaning (Dedner et al., 2003) and eight-wave scheme (Powell et al., 1999) are also used to keep the magnetic field divergence-free.

The Hall MHD equations (with a separate electron pressure equation) to be solved are

$$\frac{\partial \rho}{\partial t} = -\nabla\cdot(\rho\mathbf{u}) \tag{1}$$

$$\frac{\partial(\rho\mathbf{u})}{\partial t} = -\nabla\cdot\left[\rho\mathbf{u}\mathbf{u}+(p+p_e)\bar{I}+\frac{B^2}{2\mu_0}\bar{I}-\frac{\mathbf{B}\mathbf{B}}{\mu_0}\right] \tag{2}$$

$$\frac{\partial e}{\partial t} = -\nabla\cdot\left[(\epsilon+p)\mathbf{u}+(\epsilon_e+p_e)\mathbf{u}_e+\mathbf{u}_e\cdot\left(\frac{\mathbf{B}^2}{\mu_0}\bar{I}-\frac{\mathbf{B}\mathbf{B}}{\mu_0}\right)-\mathbf{B}\times\eta\mathbf{j}\right] \tag{3}$$

$$\frac{\partial \mathbf{B}}{\partial t} = -\nabla\times\left[\mathbf{u}_e\times\mathbf{B}+\frac{\nabla p_e}{ne}\right] \tag{4}$$

$$\frac{\partial p_e}{\partial t} = -\nabla \cdot (p_e \mathbf{u}_e) - (\gamma - 1) p_e \nabla \cdot \mathbf{u}_e \tag{5}$$

where $\bar{I}$ is the identity matrix, ρ is the mass density, $\mathbf{u}$ is the plasma bulk velocity, $\mathbf{B}$ is the magnetic field, p_e is the electron pressure, p is the ion pressure and $\mathbf{j} = \nabla \times \mathbf{B}/\mu_\mathbf{0}$ is the current density. The Hall velocity and electron bulk velocity are defined as

$$\mathbf{v}_H = -\frac{\mathbf{j}}{ne} \tag{6}$$

$$\mathbf{u}_e = \mathbf{u} + \mathbf{v}_H \tag{7}$$

The total energy density is

$$e = \epsilon + \epsilon_e + \frac{B^2}{2\mu_0} = \frac{1}{2}\rho \mathbf{u}^2 + \frac{1}{\gamma - 1}(p + p_e) + \frac{\mathbf{B}^2}{2\mu_0} \tag{8}$$

ϵ is the hydrodynamic energy density and $\gamma = 5/3$ is the adiabatic index. Apart from $(\rho, \mathbf{u}, \mathbf{B}, p, p_e)$, other variables are derived quantities.

The continuity equation (1), momentum equation (2), energy equation (3) and electron pressure equation (5) are solved with an explicit time stepping scheme. The convection term $\mathbf{u} \times \mathbf{B}$ and pressure gradient term $\nabla p_e/ne$ are solved using explicit scheme in the induction equation (4) while the Hall term $\mathbf{v}_H \times \mathbf{B}$ is advanced with an implicit scheme. The Hall MHD equations introduce whistler mode wave, which has a characteristic wave speed inversely proportional to the wavelength. In a numerical scheme, at least two grid cells are needed to resolve the shortest wavelength, so the fastest whistler wave speed is proportional to $1/\Delta x$ while Δx is the cell size. The time step in a fully explicit scheme is limited by the Courant-Friedrichs-Lewy (CFL) condition: $\Delta t \sim \Delta x / c_{\max}$, where $c_{\max}$ is the fastest wave speed. which leads to a time step proportional to $1/(\Delta x)^2$. We use a semi-implicit scheme Tóth et al. (2012) to handle the stiff term in the induction equation, which allows the time step to be limited by the fast magnetosonic wave speed instead of the whistler speed.

A three-dimensional block-adaptive Cartesian grid is used to cover the entire computational domain: $-224R_E < x < 32R_E$, $-128R_E < y < 128R_E$, $-128R_E < z < 128R_E$ in GSM coordinate. The Hall effect is restricted to $x \in [-100R_E, 20R_E]$, $|y| < 30R_E$ and $|z| < 20R_E$ box region excluding a sphere of radius $3R_E$ centered at the Earth to speed up the simulation, (x, y, z) is defined in GSM coordinate system. The cell size of in the magnetotail is refined to the resolution with $\Delta x = 1/4R_E$. About fourteen millions cells are used in total. At the inner boundary $r = 2.5R_E$, the density is calculated by the formula $\rho_{\text{inner}} = 28 + 0.1\text{CPCP amu/cm}^3$, where CPCP is the average of the northern and southern cross polar cap potentials measured in keV. This boundary condition has been used successfully in previous geomagnetic storm simulations (Pulkkinen et al., 2013). The pressure and magnetic field $\mathbf{B}_1$ has zero gradient. The radial velocity is set to zero and the tangential velocity calculated from the Ridley Ionosphere Model (RIM) developed by (Ridley et al., 2004) is used as the velocity boundary.

2.2 Particle-in-cell Model: FLEKS

The FLexible Exascale Kinetic Simulator (FLEKS) () is used as the particle-in-cell (PIC) model (PC component in the SWMF) to resolve kinetic physics. FLEKS inherits the two-way coupling method (Daldorff et al., 2014) for coupling with BATS-R-US and the Gauss's law satisfying energy-conserving semi-implicit method (GL-ECSIM) (Y. Chen & Tóth, 2019) for the PIC solver in the MHD-EPIC method. What's more, to implement the adaptation in the MHD-AEPIC, FLEKS introduces an adaptive grid for more flexibility in covering part of the computational domain and adjusting it over time. Since the geomagnetic storm simulation is long enough to cause the number of macro particles in grid cells change significantly. FLEKS provides a particle merging and splitting

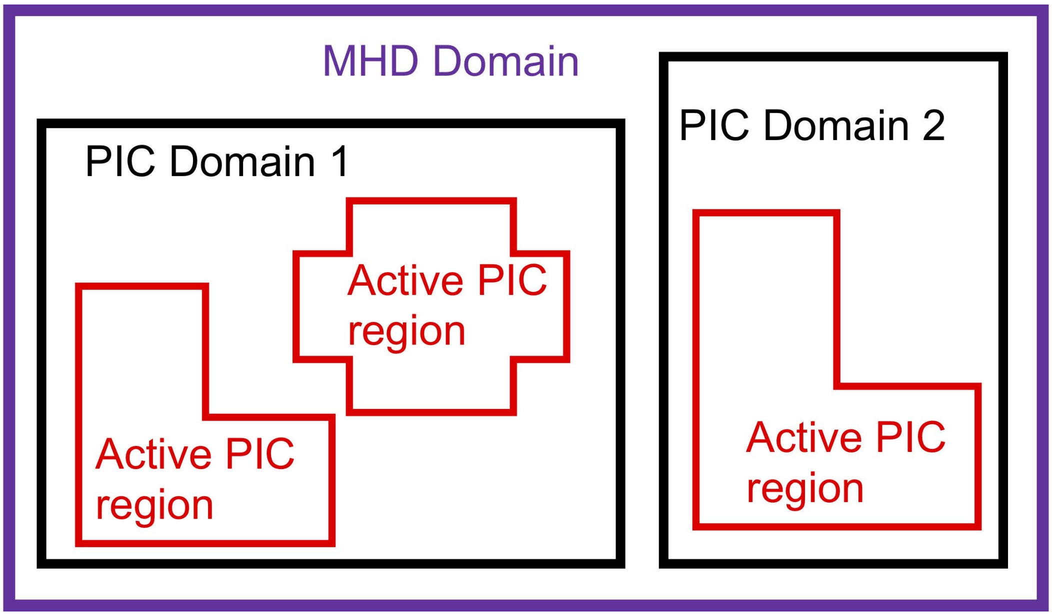

Figure 1. The schematic plot of the FLEKS adaptive grid. The red line boundary shows the flexibility of turning on and off the PIC patches during the simulation.

feature to tackle this problem: merging particles in a high particle number cell can improve load-balancing and speed up simulation while splitting particles in a low particle number cell can reduce noise for the PIC simulation. All these features are applied to the magnetic storm simulation in this paper. Figure 1 is a schematic plot of the adaptive grid which is the feature most related to the simulation in this paper, more details can be found in the work by (?, ?).

2.3 Selection Criteria of PIC Regions

As described in the previous section, FLEKS allows patches to be turned on and off during the simulation. To make the active PIC patches only cover the regions of interest, the MHD model should locate these regions and pass this information to the FLEKS. Finding the locations of magnetic reconnection sites can be done in various ways including tracing field lines ("Separator Reconnection at the Magnetopause for Predominantly Northward and Southward IMF: techniques and results", 2016). For sake of efficiency and generality, here we use a local criteria based on the magnetic field solution only.

Magnetic reconnection usually happens in current sheets where the current density j is strong and the magnetic field B is weak. In particular, the field $B_\perp$ perpendicular to the current vector $\mathbf{j} = \nabla\times\mathbf{B}$ should be close to zero, while the guide field parallel to the current can be non-zero. We define the following relation as our first criterion

$$c_1 = \frac{j\Delta x}{B_\perp + \varepsilon} = \frac{j^2\Delta x}{|\mathbf{j}\times\mathbf{B}| + j\varepsilon} \tag{9}$$

where ε is a small dimensional constant in units of the magnetic field introduced to avoid dividing by zero. We use $\varepsilon = 1$ nT in our simulations presented here which is much smaller compare to the typical magnetic field intensity in the tail current sheet. Δx is the local cell size that is used in calculating the curl of the magnetic field when obtaining the current, so that $j\Delta x$ is the jump of the transverse magnetic field between neighboring grid cells. The expression c_1 is dimensionless. We use the threshold $c_1 > 0.8$ in this work to select the cells that are close to the reconnection sites.

While this criterion works quite well in general, we sometimes find that it selects the axis of flux ropes, or O-lines, in addition to X-lines, especially if ε is very small. Reconnection does not occur at O-lines, so we developed a second criterion that distinguishes X- and O-lines based on the divergence of the magnetic field curvature vector:

$$c_2 = [\nabla \cdot (\mathbf{b} \cdot \nabla \mathbf{b})](\Delta x)^2 \tag{10}$$

where $\mathbf{b} = \mathbf{B}/|\mathbf{B}|$ is a unit vector along the magnetic field. Δx is the local cell size so that c_2 is a dimensionless value. We use $c_2 < -0.1$ to identify X-lines.

The above two criteria are identifying magnetic reconnection sites through local plasma properties in a general scenario. However, current sheets in the solar wind can also satisfy those two criteria. To make the selection more accurate, we need to introduce a third criterion to exclude the volume outside the magnetosphere. Observations show that specific entropy is two orders of magnitude larger in the magnetosphere than in the magnetosheath (X. Ma & Otto, 2014). Here we use the specific entropy as the third criterion:

$$c_3 = \frac{p}{\rho^\gamma} \tag{11}$$

where p is the plasma thermal pressure, ρ is the plasma density, and $\gamma = 5/3$ is the ratio of the specific heats (Birn et al., 2006, 2009). Different from the c_1 and c_2 introduced above, this criteria is dimensional and we use the threshold value $c_3 > 0.02\mathrm{nPa/cm}^{-3\gamma}$.

The three criteria can identify X-lines in the magnetotail well. To make the active PIC region large enough around the X-lines, we flag all patches where the criteria are met, and then activate all patches within a distance L_x, L_y and L_z from these flagged patches in the x, y and z directions, respectively. We use $L_x = 4R_E$ and $L_y = L_z = 2R_E$ in this work.

Each MPI process of BATS-R-US calculates the above criteria on their respective sub-domains overlapping with the PIC grid and activate the patches of the PIC grid. Then the processors collect the information: a PIC patch is activated if any of the BATS-R-US processes activated it. Since the status of all PIC patches (on/off) is stored in each MPI processor of BATS-R-US, using the default logical array would consume a lot of memory. To reduce the memory use, the status is stored by a single bit, which is 32 times smaller than the size of the default logical variable in Fortran. The information is conveniently collected with the bitwise "or" operator `MPI_BOR` used in the `MPI_ALLREDUCE` call.

2.4 Ionospheric Electrodynamics Model: RIM

The Ionospheric Electrodynamics (IE) is solved by the Ridley Ionosphere Model (RIM) (Ridley et al., 2004). The RIM model solves a Poisson-type equation for the electric potential on a 2-D spherical grid. In this work, the grid resolution is set to 2° on both longitude and latitude directions. The lower latitude boundary is at 10° where the electric potential is set to zero.

The BATS-R-US and RIM models are two-way coupled every 5 seconds. To calculate the Poisson-type equation, the RIM obtains the field-aligned currents (FAC) calculated at $3R_E$ from the BATS-R-US model and maps down to its grid. The F10.7 flux is also an input parameter of RIM that is used together with the FAC to calculate the particle precipitation and conductances based on an empirical model. The electric field calculated by the RIM is mapped back to the inner boundary of BATS-R-US to obtain the $\mathbf{E}\times\mathbf{B}/B^2$ velocity for its inner boundary condition. The cross polar cap potentials (CPCP) are also sent to BATS-R-US to set the density at the inner boundary. FORMULA?!

2.5 Inner Magnetosphere Model: RCM

The Inner Magnetosphere (IM) is modeled by the Rice Convection Model (RCM) (Wolf et al., 1982; Toffoletto et al., 2003). The standard RCM settings are used, including an exponential decay term to the RCM equations: the phase space density decays towards zero with a 10-hour e-folding rate. The decay term makes the Dst index recover better after large storms.

The RCM model is one-way coupled with RIM and two-way coupled with BATS-R-US every 10 seconds. In the one-way coupling from RIM to RCM, the electric potential from RIM is sent and interpolated on to the RCM grid. In the two-way coupling between BATS-R-US and RCM, the BATS-R-US identifies the closed field line regions and calculates field volume integrals of pressure and density (De Zeeuw et al., 2004). The integrated pressure and density are applied to RCM as the outer boundary condition with the assumption of 90% H^+ and 10% O^+ number density composition. From RCM to BATS-R-US, the GM grid cell centers are traced to the RCM boundary along the magnetic field lines (De Zeeuw et al., 2004) and the BATS-R-US pressure and density are pushed towards the RCM values with a 20s relaxation time.

3 Results: 3D Global Simulation with Kinetic Physics in the Magnetotail

3.1 Simulation Setup

In this paper, we applied the MHD-AEPIC method to a geomagnetic storm event on Aug. 6. 2011 with a observed minimum Dst -126 nT at 2011-08-06 03:24:00. Previous works show frequent flapping motion of the megnetotail current sheet during the storm time (Tsutomu & Teruki, 1976; Volwerk et al., 2013), so the adaptively embedding feature is perfect for only covering the current sheet during the simulation. We start our simulation at 2011-08-05 15:00:00 and end it at 2011-08-06 07:00:00. This time range covers the main phase and the early recovering phase of the storm when the largest geomagnetic impact happens. The solar wind inputs covering the simulation time are plotted in the Figure 2. The solar wind condition for the steady state is taken at 2011-08-05 15:00:00, $\mathbf{B} = (0, 1.06 \times 10^{-3}, 7.25 \times 10^{-3})$ nT, mass density 4.25 amu/cm^3, ion pressure 3.39×10^{-3} nPa and solar wind velocity $\mathbf{u} = (-425, 6.45, -9.09)$ km/s. The BATS-R-US and RIM models are turned on to reach a steady state after 50k iteration steps. The meridional plane cut of the plasma density plot of the steady state is shown in Figure 3 along with the different refinement level boundaries of the AMR grid. Then the SWMF is switched to a time-accurate mode with FLEKS and RCM models turned on. The computational domain of FLEKS is decided by the selection criteria introduced above. To compare with, we also conduct two other simulations without FLEKS: one with Hall MHD model and the other with ideal MHD model.

3.2 PIC Region Adaptation

In this subsection, we will demonstrate the adaptive embedding results of the PIC model with the MHD domain. Figure 4 illustrates PIC region is changing over the simulation runtime. Figure 4 (a)-(f) are snapshots from six different times of the geomagnetic storm simulation. The color contours are J_y on the meridional plane to show the magnetospheric current system. Boundaries of active PIC region is shown in grey isosurface. Snapshots 4 (a) and (b) are taken before the sudden commencement of the storm. At this time, the IMF B_z is pointing northward and the solar wind speed is about 400 km/s. From the isosurface plot, the PIC region is covering the tail current sheet tilting southward. In Figure 4 (b), the tail current sheet is kinked and the PIC region adjusts its shape to accommodate the tail current sheet. Snapshots 4 (c)-(f) are taken after the sudden commencement of the storm. Here we observe a much compressed magnetosphere

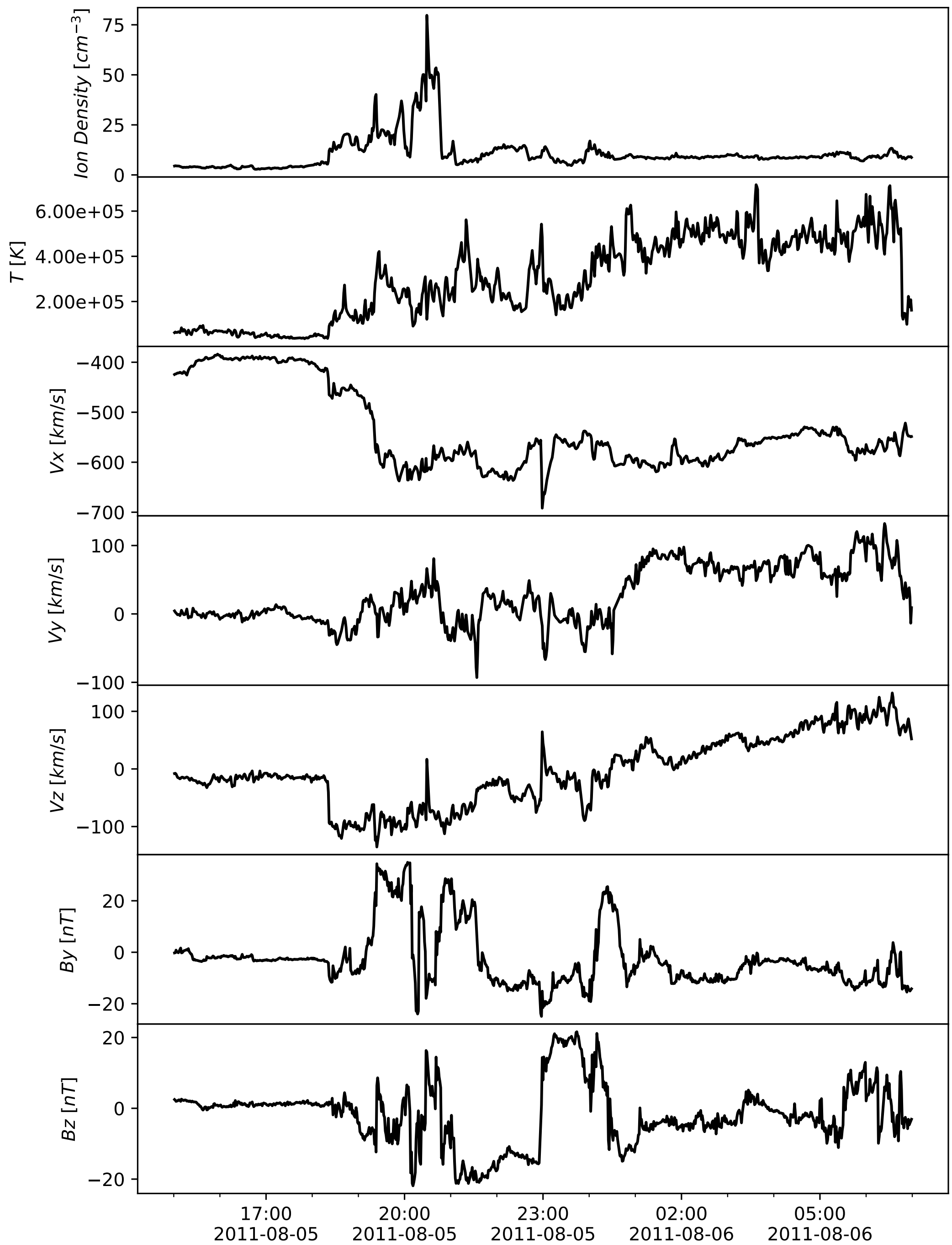

Figure 2. The solar wind bulk plasma and interplanetary magnetic field input in Geocentric Solar Magnetospheric coordinates (from top panel to the bottom: plasma density, plasma temperature, x, y and z components of the plasma flow velocity, y and z components of the magnetic field) for the simulation in this paper. The x-component of the magnetic field is set to be 0. The solar wind data is obtained from the ACE spacecraft observation and propagated to the bow shock position (Pulkkinen et al., 2013).

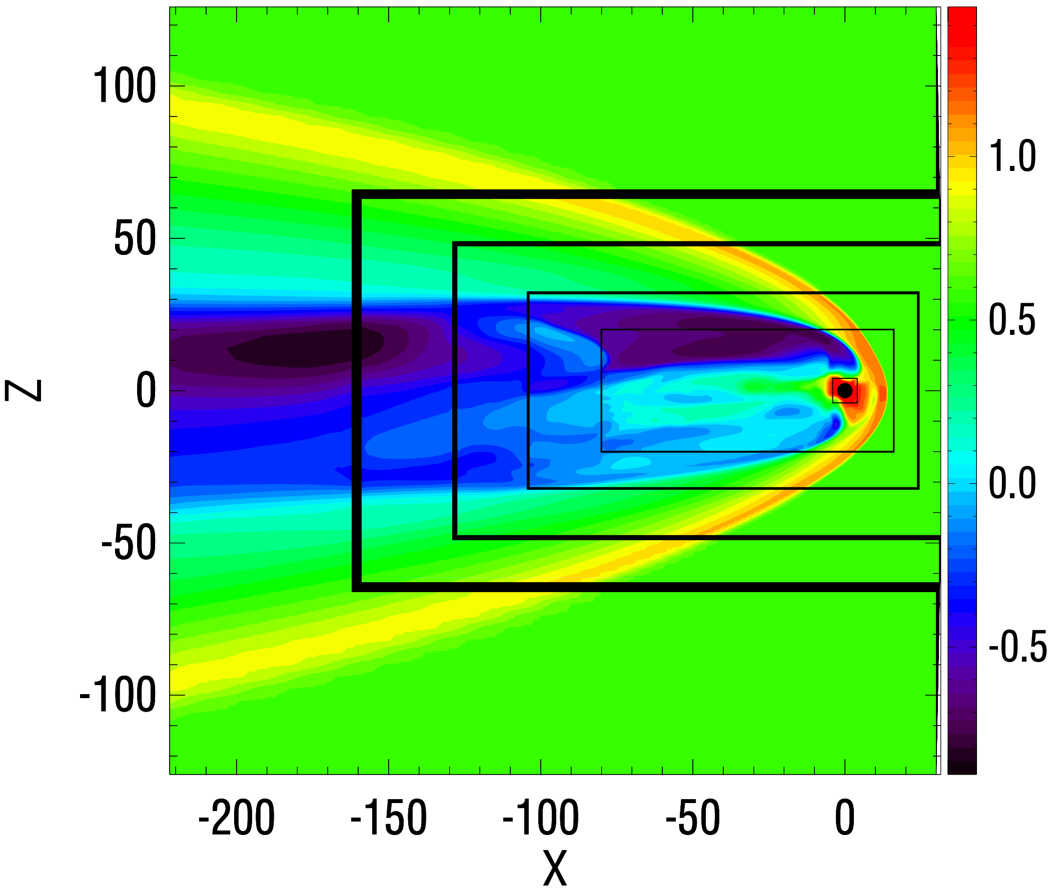

Figure 3. The meridional plane of the simulation domain. The color contour shows the plasma density of the steady state on a logarithmic scale. The black lines are the boundary of grid cells at different refinement level. The cell size can also be distinguished by the thickness of the lines. The resolution at the square region near earth is 1/8 R_E and grid resolution at magnetotail is 1/4 R_E. The refinement ratio between two adjacent levels is 2.

as well as an enhanced current density. In the last two snapshots, the tail current sheet is tilting northward and it is well covered by the PIC region. From the snapshots, we can conclude that the PIC region selection criteria work well in identifying the tail current sheet, which can make the PIC region accommodate with the flapping motion of the magnetotail. The red line in Figure 4 (g) is the volume of the active PIC region (smoothed every 60 seconds), the Dst index is also presented in the background for reference. The volume of the PIC region increase after the sudden commencement and start dropping at the recovering phase. This reflects the tail current system intensity related to the solar wind condition. Notice that the volume is less than 2000 R_E^3 for the entire storm simulation, which is only about 1.4% of a large PIC box extend from $-100R_E$ to $-10R_E$ on x direction and $-20R_E$ to $20R_E$ on y and z direction. This implies that the MHD-AEPIC method saves the computational resources substantially.

3.3 Global Scale Feature: Geomagnetic Indices

After demonstrating the PIC region adaptation in the previous subsection, we will compare the model output with the observation at different physical scales in the following subsections. To evaluate the models' performance on the global scale, we use the SYM-H and SME as evaluation metrics. The SYM-H uses six ground magnetometer stations to calculate the symmetric portion of the horizontal component magnetic field near the equator, which is a measurement of the ring current strength weakens the Earth's dipolar magnetic field (Ganushkina et al., 2017). The SYM-H is considered as an indicator of storm activity happening in the magnetosphere. The SuperMAG electrojet index (SME) is considered as an indicator of substorms and auroral power (Newell & Gjerloev, 2011) . SME utilizes more than 100 ground magnetometer stations at geomagnetic latitudes between $+40°$ and $+80°$ degrees which resolves the large and extreme events more effectively than the traditional Auroral Electrojets (AE) index (Davis & Sugiura, 1966; Bergin et al., 2020).

In our model, the simulated SYM-H is calculated by evaluating the Biot-Savart integral at the center of the Earth from all currents in the simulation domain. However, it's more complicated in terms of calculating SME: the magnetic field disturbances are interpolated to the positions of the ground magnetometer stations and the simulated SME is calculated following the method defined by SuperMAG. From Figure 5, the MHD-AEPIC produces geomagnetic indices close to other two MHD models. The initial, main and recover phases for the storm event are all been reproduced by three models from the SYM-H plot. However, the models cannot produce the lowest SYM-H which corresponds to the strongest observed geomagnetic perturbations. This feature can also be observed from the SME: all three models produce increased auroral electrojets, however the second and third enhancement are weaker than observation. The geomagnetic indices demonstrate that by introducing kinetic physics in the magnetotail, the global configuration of the simulated magnetosphere will not be changed much from the MHD solutions. It is to be seen if this trend persists for other storms, especially extreme events.

3.4 Mesoscale Feature: Flux Ropes

After verifying the geomagnetic indices generated from the simulated magnetosphere, we will illustrate the characteristic of flux ropes as a mesoscale feature from the tail reconnection dynamics. Figure 6 shows the magnetosphere simulation results from three models at the same time 2011-08-05 19:40:00. Figure 6 (a1), (b1) and (c1) are parts of the meridional planes from MHD-AEPIC, Hall MHD and ideal MHD. Here the magnetotail region where $-80R_E < x < -5R_E$ and $-20R_E < y < 10R_E$ are plotted. Since three snapshots are taken at the same time, the global configurations of the magnetosphere share a lot of similarities although with several differences. All three models give a southward tilted magnetotail which is compressed most on the z direction at around $x = -40R_E$ as a result of the IMF structure. In terms of the reconnection feature, all

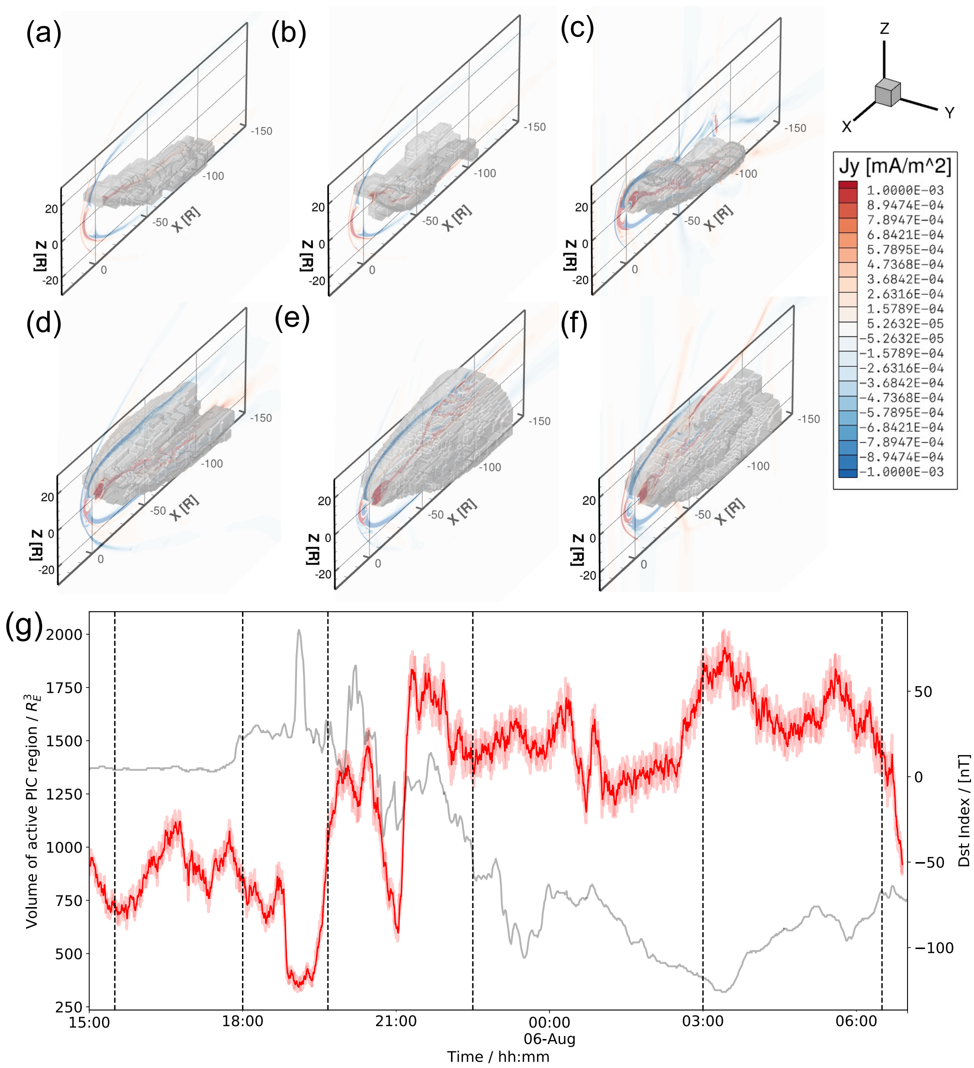

Figure 4. (a-f) Demonstrations of PIC region adaptation during the simulation runtime. The contour plot of the J_y on meridional plane is showing the general condition of the magnetospheric current system. The active PIC region boundary is shown by a grey isosurface. (g) The change of the active PIC region volume (in R_E^3) during the runtime. The Dst index is colored in grey for reference. The six vertical dashed lines correspond to the times of the snapshots (a)-(f), respectively.

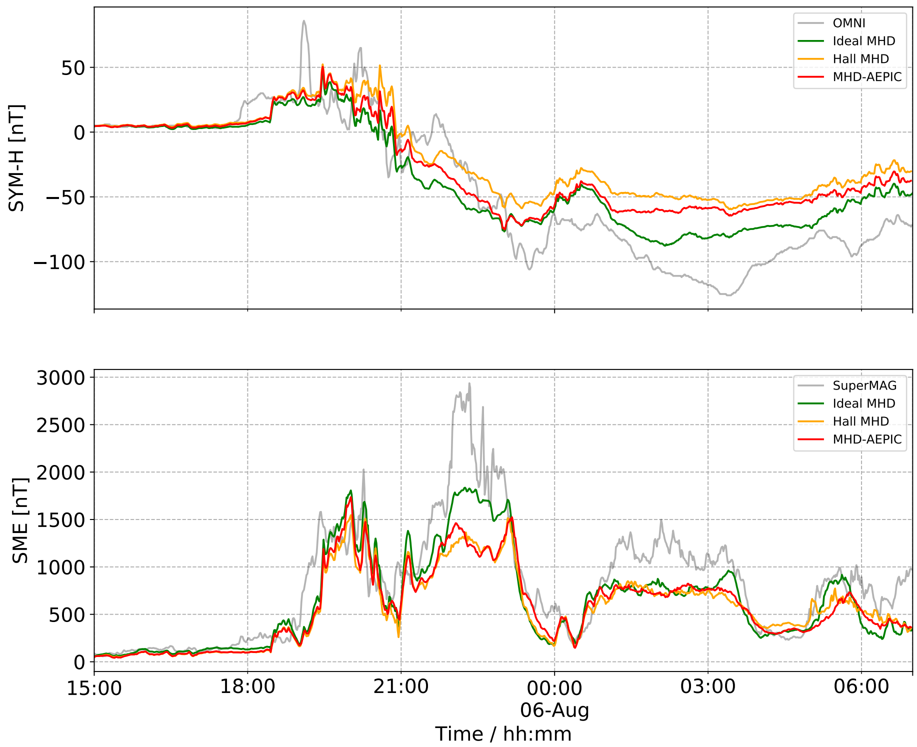

Figure 5. Aug. 6 2011 storm. Colored lines show the SYM-H and SuperMAG electrojet index (SME) from three different models and the grey line is from the observational data.

three models generate X-line on the tail current sheet at around $x = -20R_E$ and $y = -5R_E$. Diverging reconnection ion jets are generated at the major X-line for all three models, but the ideal MHD simulation generate much faster earthward ion flow speed (>1000 km/s) compared to other two models ($\approx$ 400 km/s) on the meridional plane. To analyze physical quantities on the current sheet better, we extract the current sheet surface by defining an isosurface where $B_x = 0$ and project this surface on the $x-y$ plane. The structures on the dawn-dusk direction can be observed in these current sheet surface plots. Figures 6 (a5)-(c5) are contour plots of the current sheet z coordinate. The z coordinates on the current sheet surface agree well with the meridional plane plot: the current sheets are at $z \approx 0R_E$ near Earth and at $z \approx -15R_E$ at far tail for MHD-AEPIC and Hall MHD models while $z \approx -12R_E$ for ideal MHD. Figure 6 (a2)-(c2) are the ion bulk flow speed plotted on the current sheet surface. The differences of the earthward ion flow structures on the dawn-dusk sides from three models can be observed on the current sheet plots. For the ideal MHD, the earthward ion flow is distributed symmetrically on the dawn and dusk sides in $[-3, 3]R_E$. The earthward ion jet generated by Hall MHD can only be observed on the dawn side with y direction coverage of $[-5, 0]R_E$. Moreover, the maximum earthward ion flow speed is also over 1000 km/s which is not on the meridional plane. The MHD-AEPIC produces earthward ion jet both on the dawn and dusk sides. However, the ion jets on the dawn side is further away from the earth while closer to the earth on the dusk side. Also, the earthward ion jets can be observed from $-5R_E$ to $7R_E$ on the y direction, which agrees with the observations that earthward flows are observed on a wide range on y direction(Angelopoulos et al., 1994).

Although the earthward ion flow from MHD-AEPIC is different from pure MHD models, the similar magnetic field structure and current sheet position indicate that these snapshots from different models represent the same physical state of the magnetosphere. Hence, it is valid to examine the flux rope features based on these results. As first proposed to be formed in the Earth's magnetotail (Schindler, 1974), magnetic flux ropes are reported to be closely related to magnetic reconnection by various observations and simulations (Hones Jr et al., 1984; Slavin et al., 1989; Daughton et al., 2006; Markidis et al., 2013). Hence, it is meaningful to use the flux rope distribution to distinguish the mesoscale features generated by different models. The observational characteristics of the flux ropes are a pair of positive and negative B_z with a core magnetic field B_y in between. Hence, we plot the B_z and $|B_y|$ on the current sheet surface on Figure 6(a-c)(2-3). Figure 6 (c3) and (c4) shows only one flux rope at $-40R_E$ (circled in red) and there is no evidence indicating flux rope exists at the near earth plasma sheet from $-40R_E$ to the Earth based on the ideal MHD model results. The Hall MHD and MHD-AEPIC give very different flux rope occurrence (Figure 6 (a-b)(3-4)) from ideal MHD: there are flux ropes generated both in the earthward and tailward flows (circled in red). For the MHD-AEPIC, we circle tailward flux rope and one earthward flux rope while in the Hall MHD results, we circle one tailward, two earthward and one occurs where there is no significant ion flow. We also present the 3-D structure of the flux ropes circled in Figure 7 in which the corresponding flux ropes are pointed with red arrows. In addition to the moving directions of the flux ropes, the diameter of the flux ropes also varies: the earthward flux ropes are observed as smaller ones. This difference has been reported in a thorough analysis of Geotail observations (Slavin et al., 2003), which suggests that small, $\approx 2-5R_E$ diameter magnetic flux ropes are relatively common in the near-tail plasma sheet where $x > -30R_E$. By examining the flux ropes as a mesoscale feature, we can conclude that by resolving the reconnection physics better, the MHD-AEPIC and Hall MHD models can produce more flux ropes in the magnetotail as well as distinguish two types of the flux ropes. However, there is no evidence supporting that the MHD-AEPIC can produce better mesoscale features than the Hall MHD, since the flux ropes are way larger than the kinetic scale which PIC model is resolving.

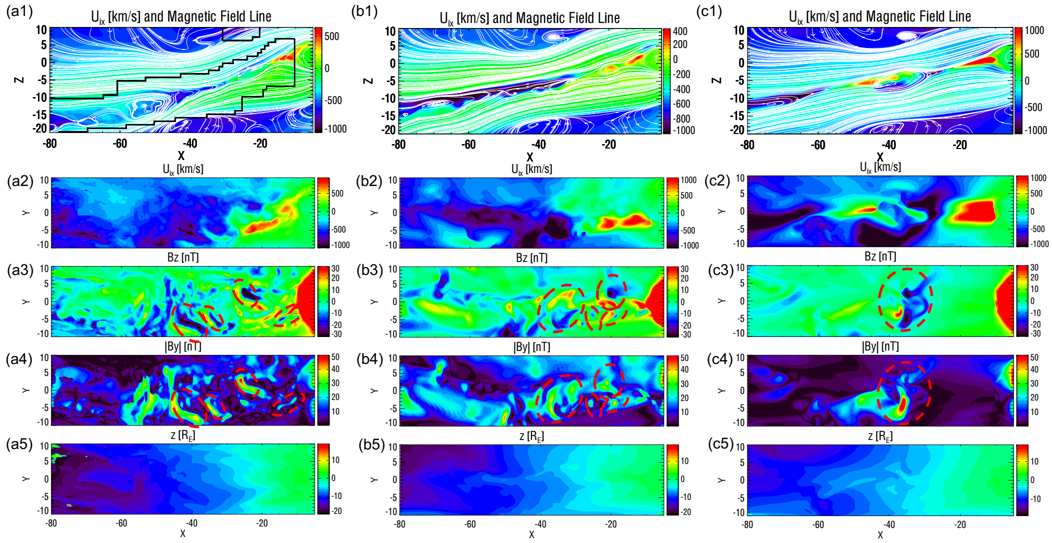

Figure 6. (a1) Ion bulk velocity and magnetic field lines on the meridional plane from the MHD-AEPIC simulation, the boundary of active PIC region is colored in black. (a2) The ion bulk velocity on the current sheet surface projected on the xy plane. (a3) The contour plot of the B_z on the current sheet surface, color saturated at ± 30 nT. (a4) The absolute value of B_y on the current sheet surface. A pair of positive and negative B_z along with a core B_y indicates a flux rope structure. (a5) The z coordinate of the current sheet surface in the unit of R_E. (b1)-(b5) are same quantities from the Hall MHD and (c1)-(c5) are from the ideal MHD. All snapshots are taken at the same time 2011-08-05 19:40:00.

3.5 Kinetic Scale Feature: Electron Velocity Distribution Function

The previous subsection shows MHD-AEPIC resolves flux rope better than ideal MHD model. In this subsection, we will demonstrate the kinetic physics in the reconnection site is also properly captured by the MHD-AEPIC. The magnetic reconnection is regarded as one of the most fundamental physical processes to transfer energy from magnetic field to plasma. Since the launch of the Magnetospheric Multiscale (MMS) mission (Burch et al., 2016), the magnetic reconnection can be resolved towards the electron scale according to multiple satellite crossings of the electron diffusion region (EDR) (Webster et al., 2018). The EDR encounters exhibits electron agyrotropy, which can be recognized by a crescent-shaped electron distributions (Torbert et al., 2018).

Figure 8 (a) is a contour plot of ion bulk velocity on the meridional plane. The ion jets in the outflow region is reflected by the color which is also a signature of the magnetic reconnection (Paschmann et al., 2013). Figure 8 (b) and (c) shows the electron velocity distribution function (VDF) from the model and the MMS observation. The VDF of the electrons is collected inside a ellipsoid region which centers at $(-30.6, 0.5, -0.9)$ R_E, the principle semi-axes are $(0.3, 2.5, 0.3)$ R_E on the (x, y, z) directions. The choice of the ellipsoid shape collects more particles near the center of the reconnection site while less when extended on the y direction. The red circle on the Figure 8 (b) is the cross section of the ellipsoid on the meridional plane. To compare with, observation by MMS3 (Hwang et al., 2019) at $(-18.1, 7.30, 0.66)$ R_E is presented aside. Although the simulation and observation are not at same time and the EDR is not at the same coordinate, the electron data is collected at the same location relative to the X-point. Also, the $y-z$ coordinates from the simulation is closely aligned with the $M-N$ coordinates from the observation (See Figure 2 (b) in Hwang et al. (2019)). This suggests that we can di-

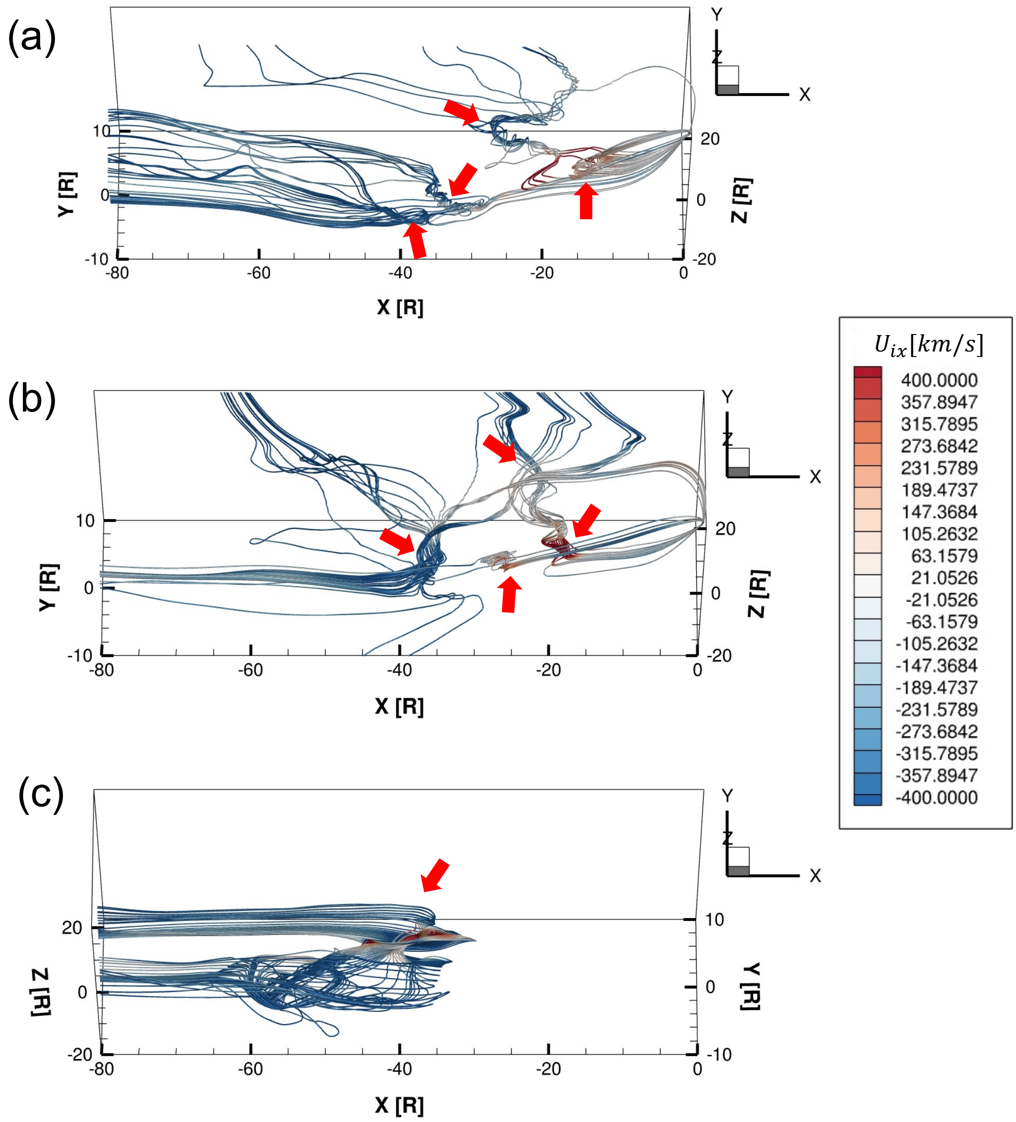

Figure 7. The 3-D flux ropes structure from three models at the same time in Figure 6. From (a) to (c) are MHD-AEPIC, Hall MHD and ideal MHD. The flux ropes are pointed with red arrows correspondingly. The magnetic field lines are colored with ion velocity U_{ix} (km/s).

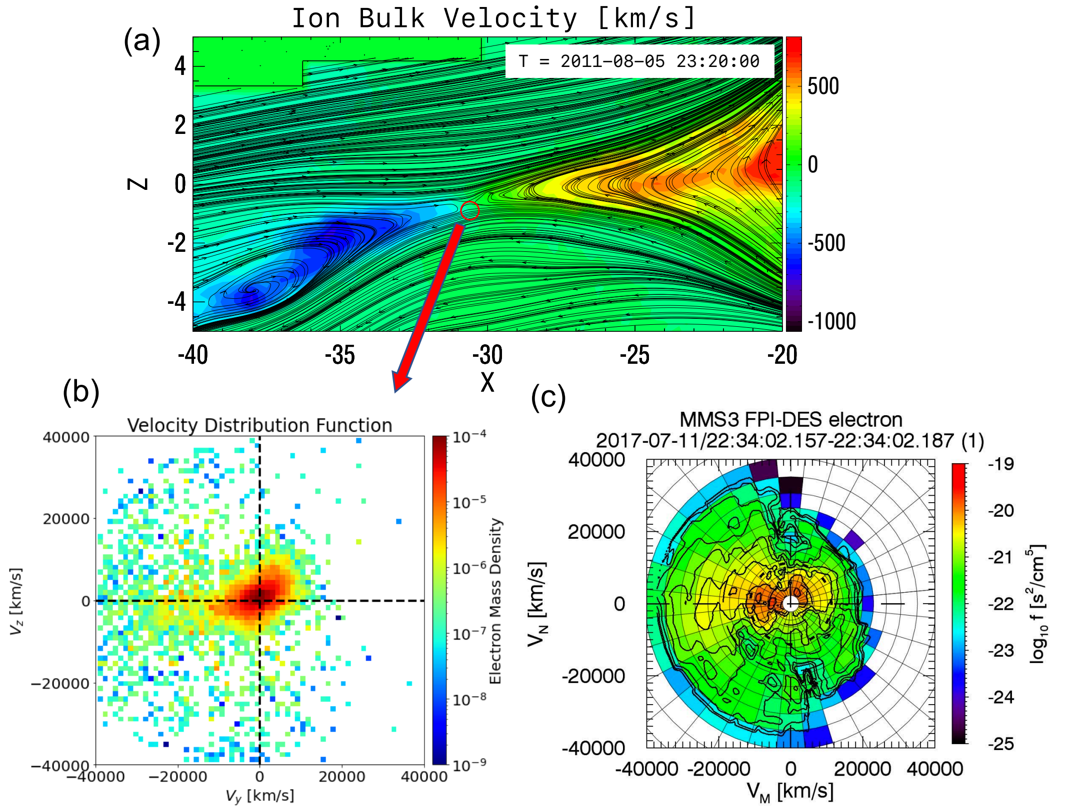

Figure 8. (a) The contour plot of the ion bulk velocity overplotted with magnetic field lines. The 2D cut is taken on the meridional plane. The red rectangle is the position where the electrons for the VDF are collected. Notice that some area at upper left is not covered by PIC which illustrates the AEPIC feature. (b) The electron VDF from the simulation, colored in electron mass density in log scale. (c) MMS3 observation (Figure 2 (c) in Hwang et al. (2019)).

rectly compare the two VDF plots. First, the electrons from the simulation is clustered in $-y$ direction and expanded evenly on z direction. The velocity ranges from ± 40000 km/s on z direction and $(-40000, 20000)$ km/s on y direction, which agrees well with the observation in Figure 8 (c). Second, a non-Maxwellian distribution can be clearly identified from the VDF both in Figure 8 (b) and (c). The electron velocity in this part expands from -20000 km/s to 10000 km/s on y direction while on z direction, it distributes evenly in ± 10000 km/s. This non-Maxwellian distribution also agrees well with the observation. This demonstrates a electron temperature anisotropy in simulated EDR, which is also recognized as a crescent distribution in Hwang et al. (2019). Hence, we can conclude that our model agrees well with observation on reproducing electron phase space distribution, which is the smallest scale in reconnection physics.

4 Conclusions and Discussions

In this paper, we introduce a newly developed magnetohydrodynamic with adaptively embedded particle-in-cell (MHD-AEPIC) model. The MHD-AEPIC allows PIC regions be turned on and off during the simulation based on the physical criteria provided. Different from the previous MHD-EPIC model which requires a fixed Cartesian box to cover the PIC region, the MHD-AEPIC model enables PIC regions moving with the reconnection sites to save computational resources substantially. We also introduce three physical based criteria to identify the magenetotail reconnection regions. To demonstrate the feasibility of the MHD-AEPIC model, we perform a geomagnetic storm event simulation with kinetic physics embedded for the first time. The flapping motion of the magnetotail current sheet during the geomagnetic storm will emphasize the advantange of the adaptation feature of the MHD-AEPIC model. We also simulate the same event using Hall MHD and ideal MHD models to illustrate what are the influences on multiple physical scales by introducing kinetic model in the magnetotail.

We examine the global scale features by comparing the SYM-H and SME indices which reflects the equatorial and auroral region disturbances. All three models properly capture the global scale disturbances such as the main phase of the storm or increase of the auroral electrojet. However, all three models fail to produce the strongest intensity for the geoindies. Hence no significant difference is found among the geoindices generated by three different models for this event. This indicates that the global magnetosphere configuration from the three models are very close, the kinetic model embedded in the magnetotail doesn't improve the global scale feature for this geomagnetic storm. If this trend persists for other storms, especially extreme events, is still to be investigated.

We analyze the mesoscale features by investigating the flux ropes produced by three models in the magnetotail. Only one major flux rope can be observed from the ideal MHD simulation at the selected time, while Hall MHD and MHD-AEPIC produce both tailward and earth-ward fluxropes. The difference of the spatial scales of two types of fluxropes is also reproduced, which is reported by various observations.

We demonstrate the electron scale kinetic physics is also reproduced by the model. The electrons are collected at the same location as the MMS observation related to the reconnection X-line. The crescent distribution of electron velocity is observed both from the model and MMS observation.

In this paper, the MHD-AEPIC has been firstly successfully applied to geomagnetic storm simulation. The adaptation feature is tested on the moving reconnection X-line with the flapping motion of the magnetotail current sheet during the geomagnetic storm. We expect the novel MHD-AEPIC model can be applied in cases which needs a moving kinetic region in a wide range.

Acknowledgments

This work was primarily supported by NSF PRE-EVENTS grant No. 1663800 and NSF-DMS 1811083. We also acknowledge support from the NASA DRIVE Center at the University of Michigan under grant NASA 80NSSC20K0600. We thank Dr. Qusai Al Shidi for the script calculating the SME index using interpolated magnetometer data from the BATS-R-US. We acknowledge the Texas Advanced Computing Center (TACC) at The University of Texas at Austin for providing HPC and storage resources that have contributed to the research results reported within this paper.

References

Angelopoulos, V., Kennel, C. F., Coroniti, F. V., Pellat, R., Kivelson, M. G., Walker, R. J., … Gosling, J. T. (1994). Statistical characteristics of bursty bulk flow events. *J. Geophys. Res.*, *99*, 21,257.

Bergin, A., Chapman, S. C., & Gjerloev, J. W. (2020). Ae, dst, and their supermag counterparts: The effect of improved spatial resolution in geomagnetic indices. *Journal of Geophysical Research: Space Physics*, *125*(5), e2020JA027828.

Birn, J., Hesse, M., & Schindler, K. (2006). Entropy conservation in simulations of magnetic reconnection. *Physics of plasmas*, *13*(9), 092117.

Birn, J., Hesse, M., Schindler, K., & Zaharia, S. (2009). Role of entropy in magnetotail dynamics. *Journal of Geophysical Research: Space Physics*, *114*(A9).

Brecht, S., Lyon, J., Fedder, J., & Hain, K. (1981). A simulation study of east-west IMF effects on the magnetosphere. *Geophys. Res. Lett.*, *8*, 397–400.

Brecht, S., Lyon, J., Fedder, J., & Hain, K. (1982). A time-dependent three-dimensional simulation of the earth's magnetosphere: Reconnection events. *J. Geophys. Res.*, *87*, 6098–6108.

Burch, J. L., Torbert, R. B., Phan, T. D., Chen, L.-J., Moore, T. E., Ergun, R. E., … Chandler, M. (2016). Electron-scale measurements of magnetic reconnection in space. *Science*, *352*, 6290. doi: 10.1126/science.aaf2939

Chen, L.-J., Hesse, M., Wang, S., Gershman, D., Ergun, R., Pollock, C., … others (2016). Electron energization and mixing observed by mms in the vicinity of an electron diffusion region during magnetopause reconnection. *Geophysical Research Letters*, *43*(12), 6036–6043.

Chen, Y., & Tóth, G. (2019). Gauss's law satisfying energy-conserving semi-implicit particle-in-cell method. *J. Comput. Phys.*, *386*, 632. doi: 10.1016/j.jcp.2019.02.032

Chen, Y., Tóth, G., Cassak, P., Jia, X., Gombosi, T. I., Slavin, J., … Peng, B. (2017). Global three-dimensional simulation of earth's dayside reconnection using a two-way coupled magnetohydrodynamics with embedded particle-in-cell model: initial results. *J. Geophys. Res.*, *122*, 10318. doi: 10.1002/2017JA024186

Chen, Y., Tóth, G., Jia, X., Slavin, J. A., Sun, W., Markidis, S., … Raines, J. M. (2019). Studying dawn-dusk asymmetries of mercury's magnetotail using mhd-epic simulations. *Journal of Geophysical Research: Space Physics*, *124*(11), 8954-8973.

Daldorff, L. K. S., Tóth, G., Gombosi, T. I., Lapenta, G., Amaya, J., Markidis, S., & Brackbill, J. U. (2014). Two-way coupling of a global Hall magnetohydrodynamics model with a local implicit Particle-in-Cell model. *J. Comput. Phys.*, *268*, 236. doi: 10.1016/j.jcp.2014.03.009

Daughton, W., Scudder, J., & Karimabadi, H. (2006). Fully kinetic simulations of undriven magnetic reconnection with open boundary conditions. *Physics of Plasmas*, *13*(7), 072101.

Davis, T. N., & Sugiura, M. (1966). Auroral electrojet activity index ae and its universal time variations. *Journal of Geophysical Research*, *71*(3), 785–801.

De Zeeuw, D., Sazykin, S., Wolf, R., Gombosi, T., Ridley, A., & Tóth, G. (2004). Coupling of a global MHD code and an inner magnetosphere model: Initial results. *J. Geophys. Res.*, *109*(A12), 219. doi: 10.1029/2003JA010366

Dedner, A., Kemm, F., Kröner, D., Munz, C., Schnitzer, T., & Wesenberg, M. (2003). Hyperbolic divergence cleaning for the MHD equations. *J. Comput. Phys.*, *175*, 645–673.

Dessler, A., Hanson, W., & Parker, E. (1961). Formation of the geomagnetic storm main-phase ring current. *Journal of Geophysical Research*, *66*(11), 3631–3637.

Feldstein, Y. I., Grafe, A., Gromova, L., & Popov, V. (1997). Auroral electrojets during geomagnetic storms. *Journal of Geophysical Research: Space Physics*, *102*(A7), 14223–14235.

Ganushkina, N., Jaynes, A., & Liemohn, M. (2017). Space weather effects produced by the ring current particles. *Space Science Reviews*, *212*(3), 1315–1344.

Glocer, A., Tóth, G., Ma, Y. J., Gombosi, T., Zhang, J.-C., & Kistler, L. M. (2009). Multifluid Block-Adaptive-Tree Solar wind Roe-type Upwind Scheme: Magnetospheric composition and dynamics during geomagnetic storms – initial results. *J. Geophys. Res.*, *114*, A12203. doi: 10.1029/2009JA014418

Haiducek, J. D., Welling, D. T., Ganushkina, N. Y., Morley, S. K., & Ozturk, D. S. (2017). Swmf global magnetosphere simulations of january 2005: Geomagnetic indices and cross-polar cap potential. *Space Weather*, *15*(12), 1567–1587.

Hamilton, D. C., Gloeckler, G., Ipavich, F., Stüdemann, W., Wilken, B., & Kremser, G. (1988). Ring current development during the great geomagnetic storm of february 1986. *Journal of Geophysical Research: Space Physics*, *93*(A12), 14343–14355.

Hones Jr, E., Birn, J., Baker, D., Bame, S., Feldman, W., McComas, D., ... Tsurutani, B. (1984). Detailed examination of a plasmoid in the distant magnetotail with isee 3. *Geophysical research letters*, *11*(10), 1046–1049.

Hwang, K.-J., Choi, E., Dokgo, K., Burch, J., Sibeck, D., Giles, B., ... others (2019). Electron vorticity indicative of the electron diffusion region of magnetic reconnection. *Geophysical research letters*, *46*(12), 6287–6296.

Janhunen, P. (1996). GUMICS-3: A global ionosphere-magnetosphere coupling simulation with high ionospheric resolution. In *Proceedings of the ESA 1996 symposium on environment modelling for space-based applications* (pp. 233–239). ESA SP-392.

LeBoeuf, J. N., Tajima, T., Kennel, C. F., & Dawson, J. M. (1981). Global simulations of the three-dimensional magnetosphere. *Geophys. Res. Lett.*, *8*, 257–260.

Lotekar, A., Vasko, I., Mozer, F., Hutchinson, I., Artemyev, A., Bale, S., ... others (2020). Multisatellite mms analysis of electron holes in the earth's magnetotail: Origin, properties, velocity gap, and transverse instability. *Journal of Geophysical Research: Space Physics*, *125*(9), e2020JA028066.

Lyon, J., Fedder, J., & Mobarry, C. (2004). The Lyon-Fedder-Mobarry (LFM) global MHD magnetospheric simulation code. *J. Atmos. Sol-Terr. Phys.*, *66*, 1333.

Lyon, J. G., Fedder, J., & Huba, J. (1986). The effect of different resistivity models on magnetotail dynamics. *J. Geophys. Res.*, *91*, 8057–8064.

Lyons, L., & Williams, D. (1980). A source for the geomagnetic storm main phase ring current. *Journal of Geophysical Research: Space Physics*, *85*(A2), 523–530.

Ma, X., & Otto, A. (2014). Nonadiabatic heating in magnetic reconnection. *Journal of Geophysical Research: Space Physics*, *119*(7), 5575–5588.

Ma, Y., Russell, C. T., Toth, G., Chen, Y., Nagy, A. F., Harada, Y., ... others (2018). Reconnection in the martian magnetotail: Hall-mhd with embedded particle-in-cell simulations. *Journal of Geophysical Research: Space Physics*, *123*(5), 3742–3763.

Markidis, S., Henri, P., Lapenta, G., Divin, A., Goldman, M., Newman, D., & Laure, E. (2013). Kinetic simulations of plasmoid chain dynamics. *Physics of Plasmas*, *20*(8), 082105.

Markidis, S., Lapenta, G., & Rizwan-Uddin. (2010). Multi-scale simulations of plasma with ipic3d. *Mathematics and Computers in Simulation*, *80*, 1509–1519. doi: 10.1016/j.matcom.2009.08.038

Newell, P., & Gjerloev, J. (2011). Evaluation of supermag auroral electrojet indices as indicators of substorms and auroral power. *Journal of Geophysical Research: Space Physics*, *116*(A12).

Paschmann, G., Øieroset, M., & Phan, T. (2013). In-situ observations of reconnection in space. *Space Science Reviews*, *178*(2), 385–417.

Powell, K., Roe, P., Linde, T., Gombosi, T., & De Zeeuw, D. L. (1999). A solution-adaptive upwind scheme for ideal magnetohydrodynamics. *J. Comput. Phys.*, *154*, 284-309. doi: 10.1006/jcph.1999.6299

Pulkkinen, A., Rastatter, L., Kuznetova, M., Singer, H., Balch, C., Weimer, D., ... Weigel, R. (2013). Community-wide validation of geospace model ground magnetic field perturbation predictions to support model transition to operations. *Space Weather*, *11*, 369-385. doi: 10.1002/swe.20056

Raeder, J., Berchem, J., & Ashour-Abdalla, M. (1996). The importance of small scale processes in global MHD simulations: Some numerical experiments. In T. Chang & J. R. Jasperse (Eds.), *The physics of space plasmas* (Vol. 14, p. 403). Cambridge, Mass..

Raeder, J., Walker, R. J., & Ashour-Abdalla, M. (1995). The structure of the distant geomagnetic tail during long periods of northward IMF. *Geophys. Res. Lett.*, *22*, 349–352.

Ridley, A., Gombosi, T., & Dezeeuw, D. (2004, February). Ionospheric control of the magnetosphere: conductance. *Annales Geophysicae*, *22*, 567-584. doi: 10.5194/angeo-22-567-2004

Schindler, K. (1974). A theory of the substorm mechanism. *Journal of Geophysical Research*, *79*(19), 2803–2810.

Separator reconnection at the magnetopause for predominantly northward and southward IMF: techniques and results. (2016). *J. Geophys. Res.*, *120*, 5377. doi: 10.1002/2015JA021417

Shou, Y., Tenishev, V., Chen, Y., Toth, G., & Ganushkina, N. (2021). Magnetohydrodynamic with adaptively embedded particle-in-cell model: Mhd-aepic. *Journal of Computational Physics*, 110656.

Slavin, J., Baker, D., Craven, J., Elphic, R., Fairfield, D., Frank, L., … others (1989). Cdaw 8 observations of plasmoid signatures in the geomagnetic tail: An assessment. *Journal of Geophysical Research: Space Physics*, *94*(A11), 15153–15175.

Slavin, J., Lepping, R., Gjerloev, J., Fairfield, D., Hesse, M., Owen, C., … Mukai, T. (2003). Geotail observations of magnetic flux ropes in the plasma sheet. *Journal of Geophysical Research: Space Physics*, *108*(A1), SMP–10.

Sokolov, I. V., Timofeev, E. V., Sakai, J. I., & Takayama, K. (1999). On shock capturing schemes using artificial wind. *Shock Waves*, *9*, 423–426.

Toffoletto, F., Sazykin, S., Spiro, R., & Wolf, R. (2003). Inner magnetospheric modeling with the Rice Convection Model. *Space Sci. Rev.*, *107*, 175-196. doi: 10.1023/A:1025532008047

Torbert, R., Burch, J., Phan, T., Hesse, M., Argall, M., Shuster, J., … others (2018). Electron-scale dynamics of symmetric magnetic reconnection diffusion region in space. *Science*, *362*(6421), 1391–1395.

Tóth, G., Jia, X., Markidis, S., Peng, B., Chen, Y., Daldorff, L., … Dorelli, J. (2016). Extended magnetohydrodynamics with embedded particle-in-cell simulation of ganymede's magnetosphere. *J. Geophys. Res.*, *121*. doi: 10.1002/2015JA021997

Tóth, G., Ma, Y. J., & Gombosi, T. I. (2008). Hall magnetohydrodynamics on block adaptive grids. *J. Comput. Phys.*, *227*, 6967-6984. doi: 10.1016/j.jcp.2008.04.010

Tóth, G., van der Holst, B., Sokolov, I. V., Zeeuw, D. L. D., Gombosi, T. I., Fang, F., … Opher, M. (2012). Adaptive numerical algorithms in space weather modeling. *J. Comput. Phys.*, *231*, 870–903. doi: 10.1016/j.jcp.2011.02.006

Tóth, G., Zeeuw, D. L. D., Gombosi, T. I., Manchester, W. B., Ridley, A. J., Sokolov, I. V., & Roussev, I. I. (2007). Sun to thermosphere simulation of the October 28-30, 2003 storm with the Space Weather Modeling Framework. *Space Weather Journal*, *5*, S06003. doi: 10.1029/2006SW000272

Tsutomu, T., & Teruki, M. (1976). Flapping motions of the tail plasma sheet induced by the interplanetary magnetic field variations. *Planetary and Space Science*, *24*(2), 147–159.

Volwerk, M., Andre, N., Arridge, C., Jackman, C., Jia, X., Milan, S. E., … others (2013). Comparative magnetotail flapping: An overview of selected events at earth, jupiter and saturn. In *Annales geophysicae* (Vol. 31, pp. 817–833).

Webster, J., Burch, J., Reiff, P., Daou, A., Genestreti, K., Graham, D. B., … others (2018). Magnetospheric multiscale dayside reconnection electron diffusion region events. *Journal of Geophysical Research: Space Physics*, *123*(6), 4858–4878.

Wolf, R. A., Harel, M., Spiro, R. W., Voigt, G., Reiff, P. H., & Chen, C. K. (1982). Computer simulation of inner magnetospheric dynamics for the magnetic storm of July 29, 1977. *J. Geophys. Res.*, *87*, 5949-5962. doi: 10.1029/JA087iA08p05949

Wu, C. C., Walker, R., & Dawson, J. M. (1981). A three-dimensional MHD model of the Earth's magnetosphere. *Geophys. Res. Lett.*, *8*, 523–526.

Zhou, H., Tóth, G., Jia, X., & Chen, Y. (2020). Reconnection-driven dynamics at ganymede's upstream magnetosphere: 3-d global hall mhd and mhd-epic simulations. *Journal of Geophysical Research: Space Physics*, *125*(8), e2020JA028162.

Zhou, H., Tóth, G., Jia, X., Chen, Y., & Markidis, S. (2019). Embedded kinetic simulation of ganymede's magnetosphere: Improvements and inferences. *Journal of Geophysical Research: Space Physics*, *124*(7), 5441–5460.